
Article:
Liu, J., Yu, P., Chen, P. et al. (5 more authors) (2023) Microstructure, properties and fracture failure mechanism of MAG welded joints of four types of stainless steels. Engineering Failure Analysis, 150. 107326. ISSN 1350-6307

https://doi.org/10.1016/j.engfailanal.2023.107326

Microstructure, properties and fracture failure mechanism of MAG welded joints of four types of stainless steels

Jihua Liu[a, b], Pijie Yu[a], Peng Chen[a], Shitao Chen [a], Roger Lewis[b], Zhibiao Xu[a], Peng Li[a], Chenggang He[a]*

([a]School of railway tracks and transportation, Wuyi Universiy, Jiangmen, 529020, Guangdong; [b]Department of Mechanical Engineering, The University of Sheffield, Mappin Street, Sheffield, UK, S1 3JD;

**corresponding auther: Chenggang He, hechengan@126.com)*

Abstract:

In this study, four types of austenitic stainless steels (SUS 301L, SUS 304, SUS 316L and SUS 321) with different chemical compositions were butt welded by using MAG (metal active gas) welding. Unique information was gained by studying the solidification mode, microstructure and mechanical properties of the four welded joints under the same welding process, and their fracture mechanisms were analyzed from the perspective of crystallography. The results indicate that the microstructure of the four austenitic stainless steel base metals is uniformly sized equiaxed austenite with δ-ferrite distributed inside or at the boundary of austenite grains in 301L and 304 base metals. The welds of the four kinds of stainless steels solidified in an Austenitic-Ferrite (AF) mode, and the final microstructures of the 301L, 304 and 316L welds is equiaxed grains while the 321 stainless steel weld grows into a dendritic structure due to its low temperature gradient. The microstructures of the fusion zone (FZ)/fine equiaxed zone (FQZ) and heat affected zone (HAZ) of the four types of stainless steels are closely related with the solidification mode of the FZ, i.e. small FZ and HAZ regions result from the Ferrite (F) solidification mode present in the 301L and 321 welded joints. However, larger FQZ regions generate in the 304 and 316L welded joints due to the Ferrite-Austenitic (FA) solidification mode. The 304 and 316L stainless steel tend to fracture at the HAZ due to the formation of a FQZ; a large angle grain boundary formed at the weld of 301L stainless steel is the reason for its fracture, and the good anisotropy of the weld and heat affected zone of 321 stainless steel also makes it easier it to fracture in the base metal (BM). The section

hardness distribution characteristics of the four stainless steels welded joints also verify their fracture tendency.

Keywords: Stainless steel; MAG welding; Microstructure; Mechanical property; Solidification mode; Fracture mechanism

1 Introduction

Stainless steel is widely used in transportation, food, pharmaceutical, cosmetics, chemical and machinery manufacturing industries due to its excellent corrosion resistance, oxidation resistance, weldability, mechanical properties and relatively low cost [1-2]. In recent years, with the great development of the railway vehicle manufacturing industry, stainless steel has also been widely used as a structural material for lifting lugs of the vehicle cabinets. However, there are few studies on the welding performance of the typical stainless steels, for example, SUS304 and SUS316. Generally, a temperature gradient along the horizontal direction (perpendicular to welding direction) will be formed due to the differences of the substrate grain distribution state along the fusion zone (FZ), as well as the complex thermal conditions in the welding melt region. As a result, uneven residual stress distributions form [3] and the microstructure and crystal orientations of the base metal (BM) and FZ vary greatly [4-5], which affects the overall performance of the welded joint.

In order to meet the quality requirements of different welded structures, various welding techniques are used in austenitic stainless steel, such as laser welding, friction stir welding, as well as others [6-10]. However, it is still difficult to broadly apply these techniques due to their complex processes, expensive equipment, demanding requirements for welding assembly precision, and poor adaptability [11-13]. GMAW (Gas metal arc welding) is used in the production of rail vehicles due to its low cost, strong adaptability and its ability to form high-quality welds [14-15]. GMAW includes two welding processes: metal inert gas (MIG) and metal active gas (MAG), MAG is widely used to weld stainless steel. In the MAG welding process, the heat transfer mode of the metal droplets in the molten pool is easily affected by the composition and diameter of the welding wire, composition of protecting gas, arc

length, current and other parameters [16-17]. These parameters therefore affect the microstructure of stainless steel welded joints which is dictated by the temperature.

A lot of research on the heat input mode of stainless steel MAG welding has been carried out. 304 austenitic stainless steel was welded by Huang et al. [18] with low-power YAG laser MAG welding. The results showed that with an increase in welding cycles, the ferrite content decreased from 20% to 10% and its morphology changed from lath, skeleton, vermicular to reticular and the corrosion resistance of the welded joints was equivalent to the base metal. The effect of heat input on the microstructure, residual stress and corrosion resistance of 304L austenitic stainless steel welded joints was studied by Unnikrishnan et al. [19]. The results indicated that with increasing heat input, the thickness of the fusion zone interface increases, as well as the dendrite thickness/width; furthermore, the ferrite content in the weld area increased from 2% to 5%, thus resulting in a significant hardness decrease. Notably, the ferrite in the welding area prefers to grow in a {100} crystalline direction under the condition of high heat input. Luchtenberg et al. [20] studied the effect of the GMAW/CMT welding on the corrosion resistance of a duplex stainless steel surfacing layer under different power. The results showed that the proportional balance between austenite and ferrite could be broken due to the different heat input, thus affecting the corrosion resistance of the welded joint. The effect of heat input on the low temperature toughness of 316LN austenitic stainless steel has been studied by Xiao et al. [21] and they found that the volume fraction and length of dendrite crystals increased with an increase in heat input, which led to a significant decrease of low temperature impact toughness.

In summary, the welding parameters can significantly influence the heat input of the welding pool, which influences the microstructure and final properties of the welded joints. However, the microstructure and properties of the welded joints are always determined by the solidification and crystallization mode of the material [22-23]. The solidification and crystallization modes of welded joints are not only related to the welding heat input, but also closely related to the heat output of the welded area/base metal. Notably, the heat output of welded joints under the same

process parameters is generally determined by the thermal conductivity of the base metal [24]. In this paper, four types of austenitic stainless steels with different chemical compositions were butt welding under the same MAG welding process. The microstructure and properties of stainless steel welded joints were explored, as well as the relationship between fracture mechanisms and solidification modes for different welded joints. The results can not only enrich the theoretical basis of austenitic stainless steel MAG welding, but also provide technical guidance for application to the forming of railway vehicle cabinets.

2 Materials and Experimental Methods

SUS 301L, SUS 304, SUS 316L and SUS 321 stainless steel plates of 3 mm thickness and 1.0 mm diameter GMS-308LS filler wire were prepared. The SUS 301L, SUS 304, SUS 316L and SUS 321 were marked as #1, #2, #3 and #4, respectively. First, the groove (as shown in Fig. 1, from Chinese standard GB/T 985.1-2008 [25]) must be polished to remove impurities such as oil and oxide. Then, butt welding was carried out with one pass with in the 80^{o} angle groove with a 2.0 mm width gap. The molten weld metal can easily penetrate to the bottom of the weld to achieve complete welding of the butt plates, thus improving the quality of the weld. The chemical compositions of the four stainless steel base metals and welding wire are shown in Table 1, and the welding process parameters and welding methods are shown in Table 2 and Fig. 1(a), respectively. A schematic temperature distribution during a weld is shown in Fig. 1(b). It is worth noting that the thermal conductivity of #4 stainless steel is much greater than that of #1, #2 and #3 stainless steels temperatures, thus resulting in a gentle temperature gradient in the fusion zone (FZ) of the #4 welded joint.

Table 1 Chemical compositions and thermal conductivity of different materials

Materials	Chemical compositions(wt%)									Thermal conductivity
	C	Si	Mn	P	S	Cr	Ni	Mo	Ti	(TC,W/m·K,at 500℃)

#1	0.02	0.39	1.15	0.032	0.001	17.17	7.11	-	-	21.5
#2	0.04	0.51	1.17	0.026	0.001	18.24	8.00	-	-	21.5
#3	0.02	0.54	1.25	0.030	0.001	17.00	10.15	2.03	-	20.9
#4	0.04	0.68	0.96	0.025	0.001	18.00	9.00	-	0.30	22.2
GMS-308L Si	0.14	0.87	1.68	0.018	0.010	19.95	9.75	0.02	0.01	21.6

Table 2 Technical parameters of the MAG welding

Welding Current(A)	Welding Voltage(V)	Welding Speed(cm/min)	Gas flow Rate （L/min)	Shielding Gas Type
200-220	18-21	36-42	10-15	98%Ar+2%O_2

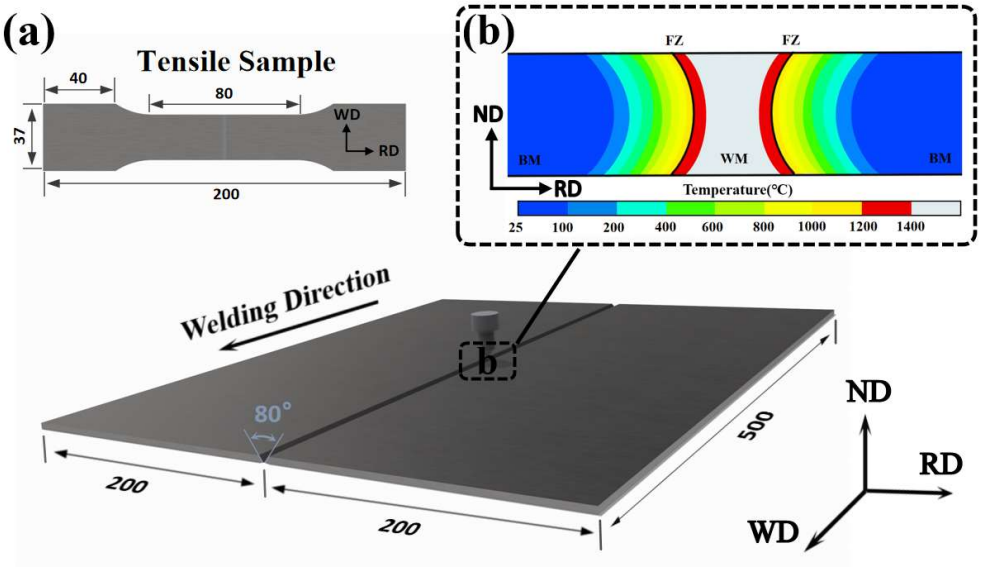

Fig. 1 (a) Schematic of welding method and tensile sample and (b) welding temperature distribution [26-28]

The microstructure of the four austenitic stainless steel base metals is shown in Fig. 2, which indicates that the equiaxed austenite in every stainless steel base metal is uniform in size. There is also visible δ-ferrite distributed inside or at the boundary of austenite grains in #1, #2 base metals. The compositions of the austenitic stainless steels presented in Table 1 indicate that the #1 base metal is a kind of metastable austenitic stainless steel, which is prone to produce a small amount of ferrite structure during its melting due to component segregation or improper processing [29-30]. On

the other hand, the δ-ferrite in #2 base metal always generates from rolling, and distributes in austenite in the form of long strips [31-32].

Metallographic samples were prepared along the sectional direction after welding, by grinding them with silicon carbide sandpaper with 240 mesh to 2000 mesh and corroding them with aqua regia (75%HCL+25%HNO_3) after polishing. The microstructure and phase structure characteristics of the four kinds of stainless steel welded joints were analyzed using an optical microscope (OM-VHX6000 3D), scanning electron microscope (SEM-Sigma 500, EDS-SEM with an Oxford-Instruments X-Max N large area SDD spectrometer), X-ray diffraction (XRD-PANalytical X'Pert powder) and electron backscatter diffraction (EBSD-HKL system interfaced with a ZEISS MERLIN Compact field-emission SEM). Tensile tests of the welded joints were also carried out at room temperature using a tensile rate of 2mm/min in an electronic universal testing machine (DNS-300).

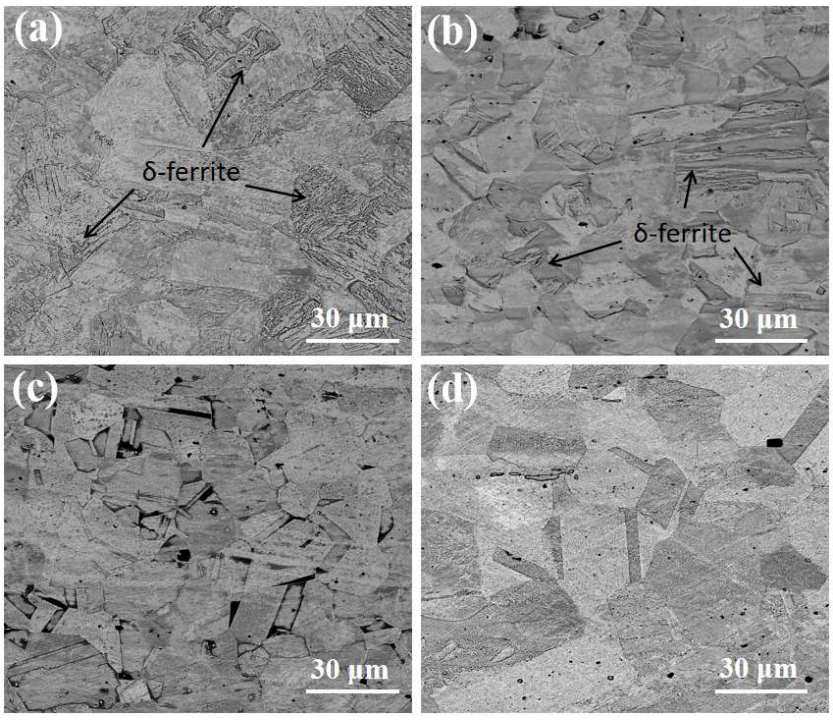

Fig. 2 Microstructure of the base metals: (a) #1; (b) #2; (c) #3; (d)#4

3 Experimental Results

3.1 Macrostructure and phase composition

Fig. 3 shows the cross-sectional macrographs of the welded joints of the four kinds of stainless steels. As can be seen, the microstructures of #1, #2 and #3 welded joints are similarly composed of equiaxed crystals (Fig. 3(a)-(c)), however, columnar crystals are visible in the #4 welded joint (as shown in Fig. 3(d)). The macrographs of the welded joints can be divided into five different areas: I Weld Metal (WM); II Fusion Zone (FZ); III Fine Equiaxed Zone (FQZ) [33]; IV Heat Affected Zone (HAZ); V Base Metal (BM).

To clarify the phase structure between the WM and HAZ, X-ray diffraction and EDS of the WM and HAZ was used to analyze their spectra and phase, the XRD phase analysis spectrum is shown in Fig. 4. The spectrum is mainly composed of austenite phase and a small amount of ferrite phase, and there are no diffraction peaks of other phases. At the same time, the height of the peaks also confirms the difference in ferrite content of the four welded joints after welding. EDS proved that the gap in the structure is Cr segregation, and the content of Ni is less, as shown in Fig. 5.

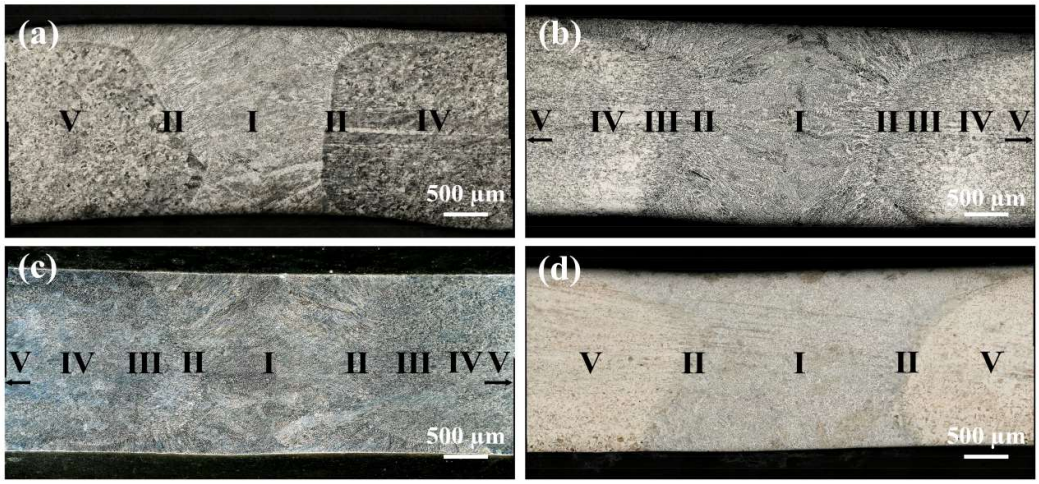

Fig. 3 Cross-sectional macrograph of four kinds of welded joints:

(a) #1; (b) #2; (c) #3; (d) #4

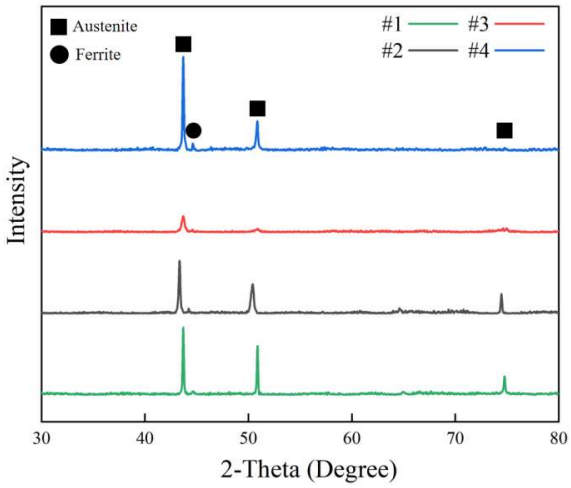

Fig. 4 Micro-area X-ray Diagrams of MAG welded joint

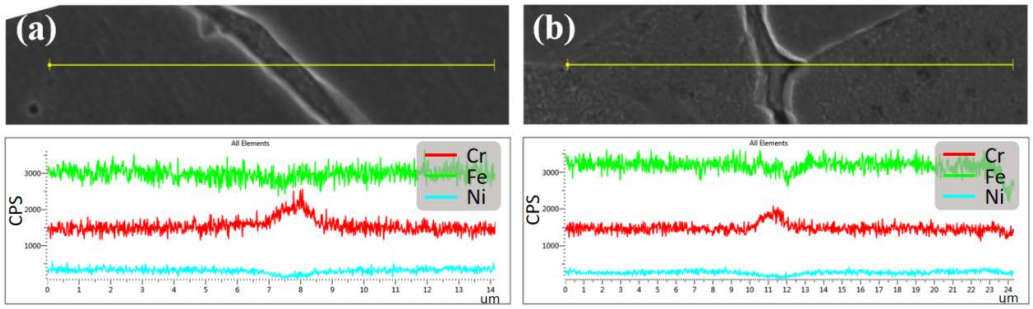

Fig. 5 EDS scan of elements at the weld [34]

3.2 Microstructure characteristics and phase analysis

Fig. 6 shows the weld microstructure of the four kinds of welded joints. The FZ and WM of #1, #2 and #3 welded joints have the same microstructure of columnar crystals and equiaxed crystals. A high temperature gradient appears at the edge of the weld due to the high thermal conductivity of the unmelted base metal near the fusion line, thus resulting in a large crystallization rate and promoting the formation of columnar crystals. The temperature gradient (from fusion line to the weld centre) in the molten pool continuously decreases and the crystallization rates of grains present a downward trend. Furthermore, an increase in the concentration of the segregated component resulting from the push of the impurity elements intensifies the slowdown of the crystallization rate. Therefore, the heat dissipation loses its directionality, and the crystal nucleus will grow freely in the liquid into equiaxed crystals [35-36].

As shown in Fig. 6(d), the microstructure of the #4 welded joint presents a dendritic morphology, which is obviously different from that of the other three welded joints. Despite the high thermal conductivity of the unmelted base metal, the microstructure of the WM of the #4 welded joint shows that the grains grow without an obvious direction, which indicates that a smaller temperature gradient occurs in the WM of the #4 welded joint, thus a needle shaped structure crystallizes finally.

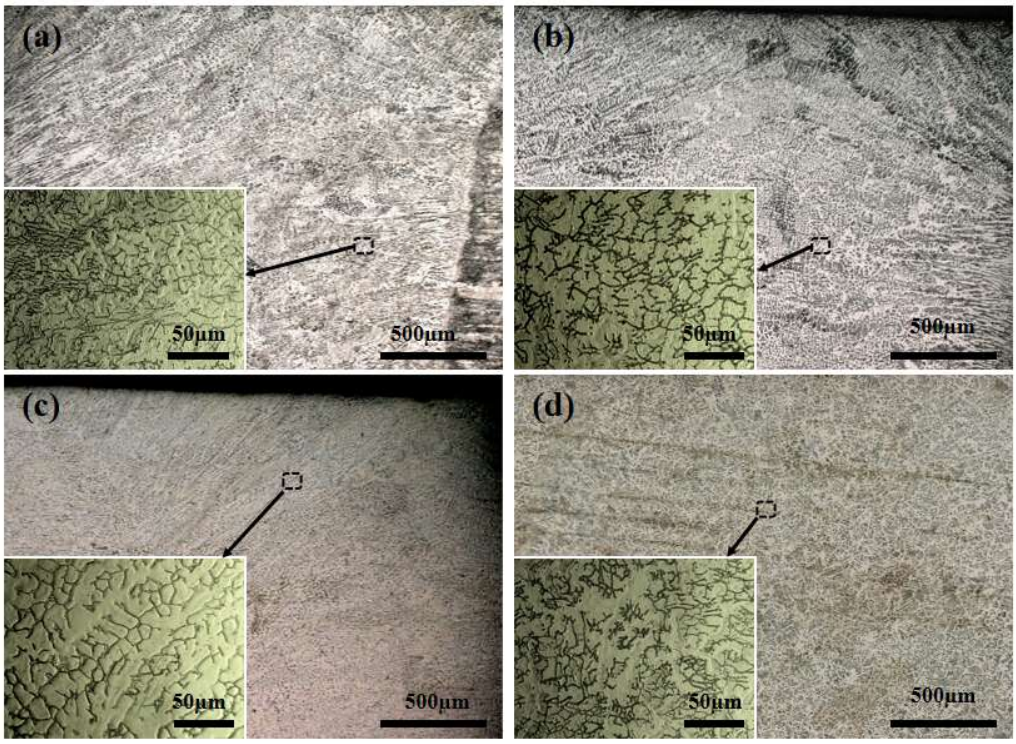

Fig. 6 Microstructure in WM of the MAG welded joints:
(a) #1; (b) #2; (c) #3; (d) #4

The microstructure for the FZ and HAZ of the four types of welded joints was observed in detail, as shown in Fig. 7. As can be seen from Fig. 7, the FZ and HAZ display different distribution states. Fig. 7(a) shows that the width of the HAZ of the #1 weld joint is relatively narrow and not clearly defined. It is mainly composed of fine columnar crystals and a small amount of cellular crystals, and the austenite grain boundary is retained during the solidification of columnar crystals [37]. There is only a fusion line in the FZs of the #2 and #3 welded joints and the FQZ areas of the #2 and #3 welded joints are much larger, as shown in Fig. 7(b) and (c). Due to the high

thermal conductivity of the base metal, the austenite in the FQZ grows into fine cellular crystals and Cr is pushed out to the grain boundary [38]. As a result, the dislocation and vacancy of chromium carbide will provide a driving force for the formation of ferrite which will grow along the rolling direction at the austenite grain boundary [39]. EDS energy spectrum scanning of the acicular seams in the HAZ of the #2 and #3 welded joints also indicates that there is an obvious Cr enrichment at the needle-like slit, that is, Cr exists in the form of solid solution in ferrite, as shown in Fig.7.

In addition, Fig. 7(d) shows that the width of the #4 HAZ is almost the same as that of #1, however, its appearance is the same as that of #2 and #3. The black precipitate phases in the WM region are densely distributed along the edge of the lath banded matrix, which results in a dendritic structure. The EDS results proved the enrichment of ferrite forming elements (such as Cr and Mo) occurs, which results in the formation of ferrite, thus the austenite promoting elements (such as Ni and C) are consumed and the formation of dendritic ferrite with concentrated distribution is promoted finally. As the heat input of the weld is finished and the under cooling rate of the weld centre is moderate, skeleton ferrite is formed.

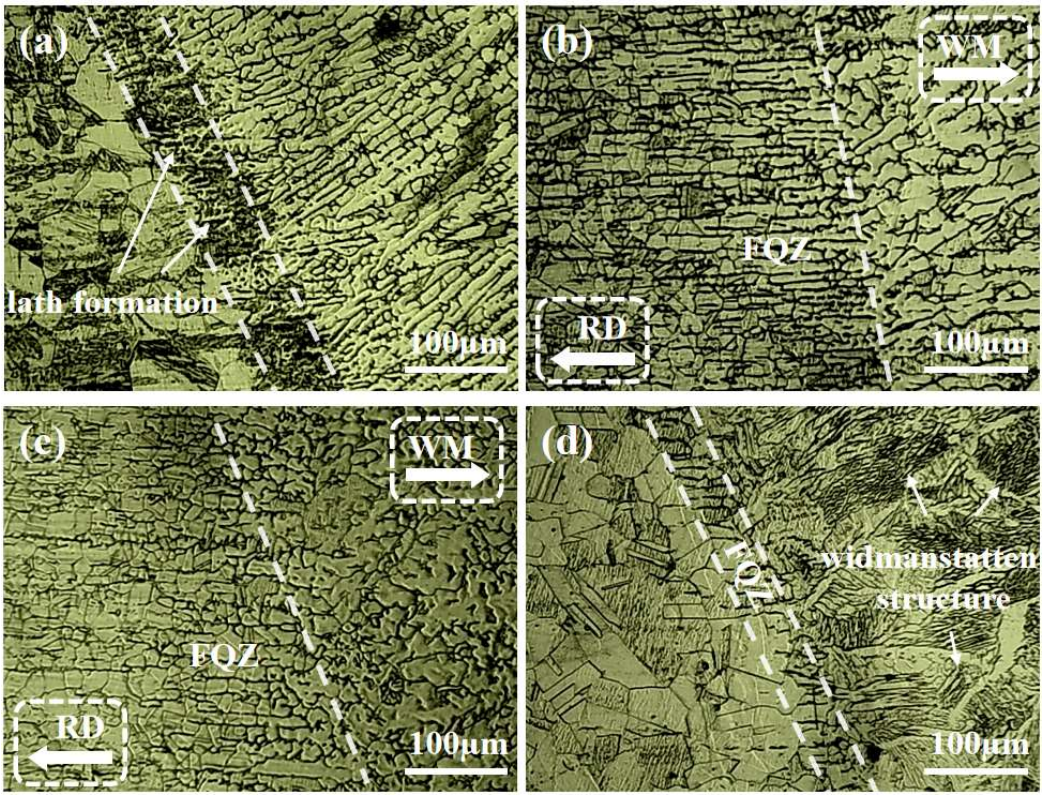

Fig. 7 Microstructures of the FZ and HAZ of MAG Welded Joints:

(a) #1; (b) #2; (c) #3; (d) #4

Fig. 8 and Fig. 9 show the orientation distribution diagrams of the Normal Direction-Rolling Direction [ND-RD] in the FZ zone and the WM zone of #1, #2, #3 and #4 samples, respectively. During the welding process, the temperature field of the FZ will change with the position of the heat source. The FZ temperature field will point from the low melting pool to the high melting pool with the welding direction, i.e. <101>. As can be seen from Fig. 8, the preferred grain orientations of the FZ zones of #1 and #4 samples are <101>, which is the main direction of the heat source. In contrast, obvious division lines occur in the direction of <001> and <101> in the FZ zone of the #2, #3 samples. As depicted in Fig. 9, the deviation angles of the weld centre of #2, #3, #4 samples are basically the same, preferring to deviate in the direction of <001>, however, the weld crystals of the #1 sample are biased towards <001> on one side and <101> on the other.

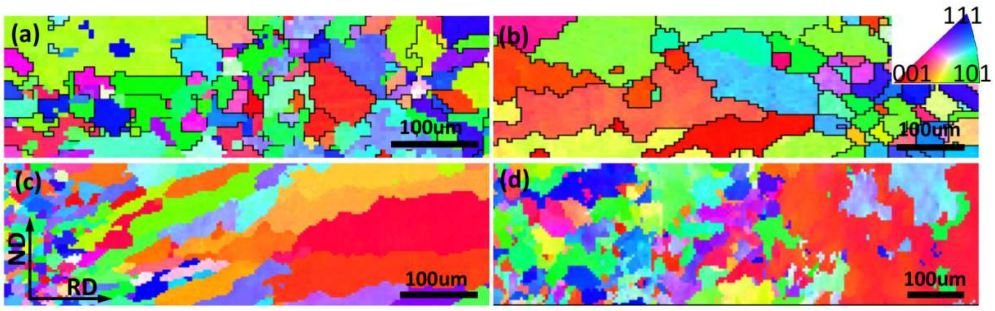

Fig. 8 IPF Maps of the FZ of MAG Welded Joints

(a) #1; (b) #2; (c) #3; (d) #4

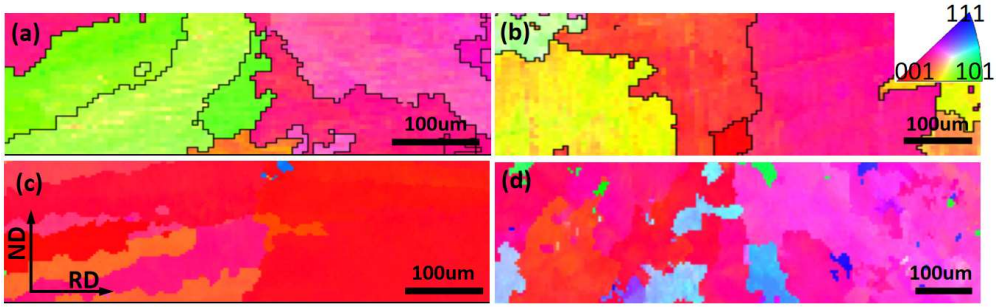

Fig. 9 IPF Maps of the WM of MAG Welded Joints

(a) #1; (b) #2; (c) #3; (d) #4

3.3 Tensile properties and fracture analysis

After the tensile tests, the macro diagrams of the four kinds of stainless steel joints are shown in Fig. 10, and obvious necking is visible in the all welded joints. Fracture will take place as the stress reaches the ultimate tensile strength [40], the fracture positions of #2 and #3 samples were at the HAZ and that of the #1 sample was at the WM. However, the #4 joint manifests a certain angle and rotated offset in the direction of the slip line after entering plastic deformation, and the fracture finally occurs in the BM.

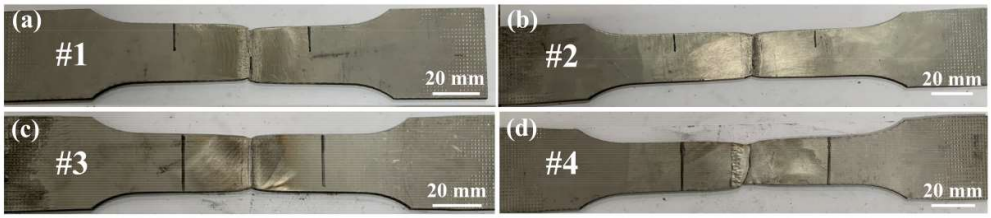

Fig. 10 Actual image of Tensile strength-experiment samples

(a) #1; (b) #2; (c) #3; (d) #4

The strain-stress responses of the four kinds of welded joints and their base metals during monotonic tensile tests are presented in Fig. 11. Interestingly, the elongations of the welded joints are related to their fracture position: the elongation is approximately 10-15% as the fracture occurs in the weld centre, such as for that of the #1 sample; furthermore, the elongations of the #2 and #3 samples will be approximately 25-35% as the welded joint fractured at the FZ. Moreover, the elongation can be up to 45-50% as the welded joint fractures at BM, as shown in Fig. 11(a). The values of mechanical properties of the four welded joints and their base metals are shown in Fig. 11(b). As can be seen from Fig. 11(b), the yield strength and tensile strength of the #2, #3 and #4 welded joints are almost the same as that of the base metal; however, the yield strength and tensile strength of the #1 base metal are much larger than that of the welded joint. Generally, the static toughness of the tensile specimen can be assessed by calculating the enclosed area of the tensile curve, which reflects the energy absorbed by a material during quasi-static stretching to fracture [41-43]. Therefore, the #2, #3 and #4 welded joints can be considered as equal strength matching, and the #1 welded joint is low strength matching, which should be avoided in engineering applications.

The morphology of the tensile fracture surfaces of the four types of samples were observed with a scanning electron microscope, as shown in Fig. 12. It can be seen from Fig. 12 that all the tensile fracture surfaces are composed of equiaxed dimples, indicating that ductile fracture occurs in each sample [44]. A small amount of secondary phase particles was generated in WM of #1, as shown in Fig. 12(a), thus resulting in the fracture surface of #1 being relatively flat, which presents less dimples and microspores. Moreover, Fig. 12(b) and (c) indicate that the fracture surfaces of the #2 and #3 welded joints are regularly staggered with many microspores distributing on their fracture surfaces. In addition, standard ductile fracture occurs at the BM of the #4 welded joint, as shown in Fig. 12(b), with a regularly staggered fracture plane and larger and deeper dimples, which will absorb more energy during the fracture process. This is because when comparing with the other welded joints, a larger grain size (as shown in Fig. 2(d) and Fig. 7(d)) and less carbides occur in the #4

BM, thus resulting in larger and deeper dimples on the staggered fracture plane.

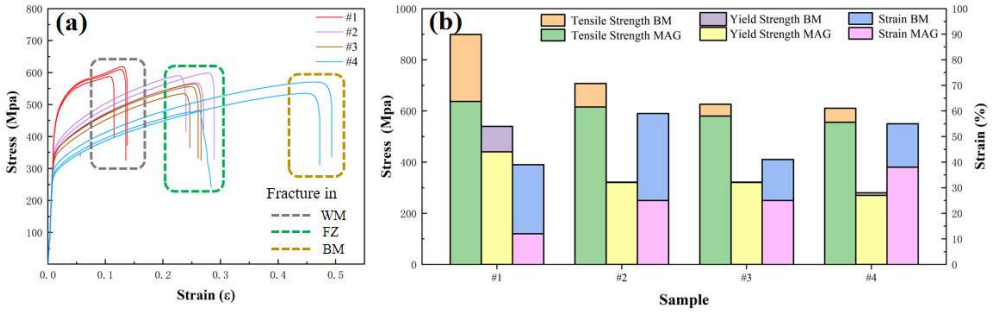

Fig. 11 Tensile properties of four welded joints

(a) Tensile curves of welded joints; (b) Mechanical properties of welded joints

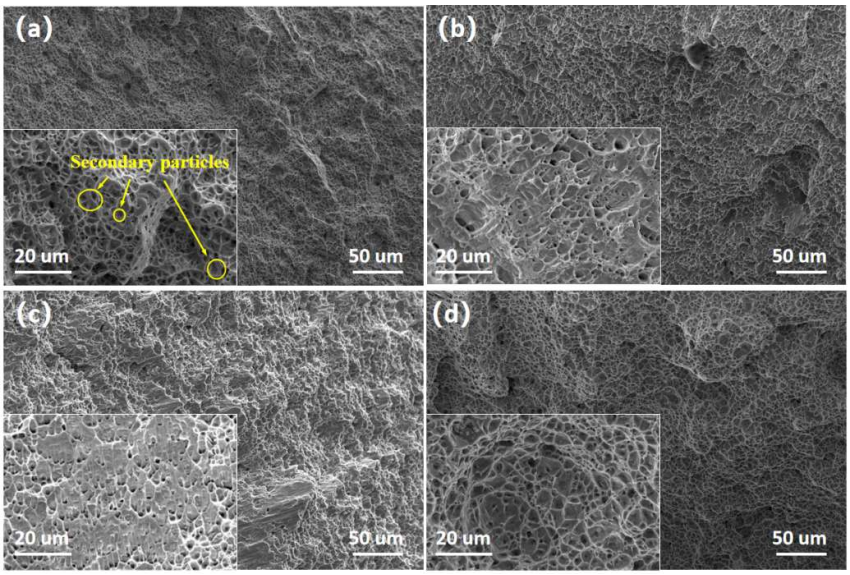

Fig.12 Topography of MAG welded joint fracture:

(a) #1; (b)#2; (c)#3; (d)#4

3.4 Microhardness

The microhardness distributions of the four welded joints are shown in Fig. 13. As can be seen from Fig. 13, the BM microhardnesses of #1, #2, #3 and #4 samples are coherent with their chemical compositions and the microhardnesses are approximately 225$HV_{0.5}$, 190$HV_{0.5}$, 170$HV_{0.5}$ and 150$HV_{0.5}$, respectively. Weld metal hardness tends to be consistent except for that of the #1 sample. According to the precipitation strengthening theory, the hard second phase particles dispersed in the

matrix always strengthen the base material, however, the strength of the material will be weakened if they appear in the form of segregation [45-46]. Obviously, the particles of this phase in #1 are uniformly dispersed, which is consistent with the results displayed in Fig. 12(a).

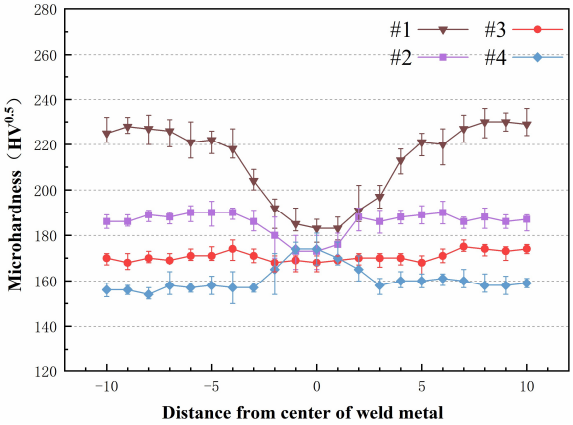

Fig. 13 Microhardness distribution of four welded joints

4 Discussion

4.1 Effect of solidification mode on microstructure of welded joints

According to the classical solidification theory, the microstructure of the metal after crystallization is mainly determined by the crystallization rate, solute concentration and the temperature gradient of the metal in the molten pool, and the ratio of temperature gradient to crystallization rate (G/R) will significantly affect the morphology of different structures in a certain range [47-48]. Three critical points of G/R are adopted to calculate the solidification mode of a metal, and the solidification route criterion can be verified by the Schneider model [49], as shown in Fig. 14. As can be seen from Fig. 14, the solidification modes in the WMs and FZs (dilution of 60% as presented in Fig. 14) in the four welded joints are AF mode and FA mode, respectively. Moreover, the F solidification mode tends to occur at the edge of the melting zone of #1 and #4 welded joints. The heat input of the four kinds of welded joints are almost the same, and the G/R of each welded joint is relevant to its Ni_{eq} and Cr_{eq}, as shown in Fig. 14, thus resulting in a difference of internal temperature gradient and finally generating different crystal morphology.

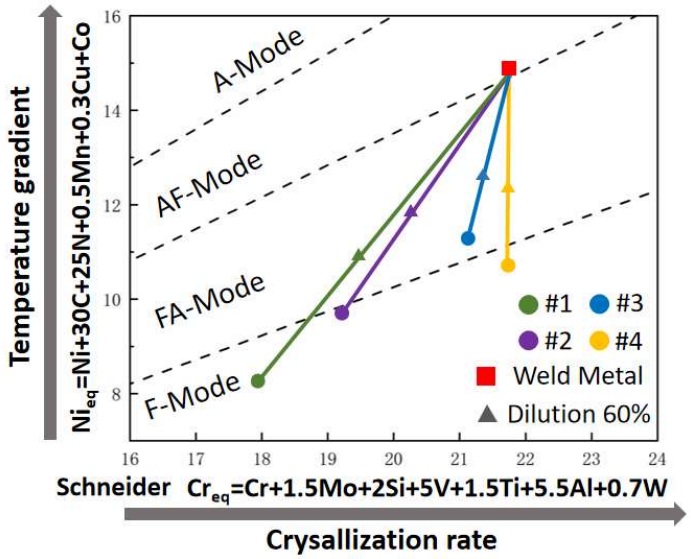

Fig. 14 Solidification roadmap of the Schneider model [49]

Moreover, the relationship between solidification mode and crystal morphology can be explained much more deeply and clearly by using a pseudo binary phase diagram of Fe-Cr-Ni, as shown in Fig. 15. The difference between Ni_{eq} and Cr_{eq} will directly affect the heat dissipation of the metal in the molten pool area, resulting in four different models of the solidification process of Cr-Ni stainless steel welds [23]. The main solidification phases of the four modes can be δ or ϒ phase and the low melting point eutectic structure presents different structures corresponding to the four solidification modes [50]. As shown in Fig. 15(b), the weld metal in the molten pool directly precipitates ϒ-austenite in an AF mode along with the temperature divergence direction, the austenite grows continuously and accumulates on both sides, thus resulting in a ferrite gap, and a large angle grain boundary is formed finally in the centre of the entire weld joint, as shown in Fig. 9. However, δ-ferrite will precipitate first in the FA or F solidification mode in the melting zone, and the detailed crystal solidification microstructures in different solidification modes are shown in Fig.15. In the FA solidification mode as shown in Fig. 15 (d), part of the energy in the molten pool will be transferred to the base metal, and ferrite will directly precipitate from the base metal, thus resulting in the formation of FQZ grains by splitting the austenite grains of the base metal. At the same time, the austenite will directly precipitate, grow

up and absorb the surrounding ferrite along the direction of the temperature gradient of the weld pool, the preliminary ferrite will be squeezed into ferrite lines. Finally, coherent columnar crystals will generate along RD and WM directions [30] as shown in Fig. 7(b) and Fig. 7(c). Moreover, in the F solidification mode, as shown in Fig. 15 (e), the energy is always retained by the preliminary δ phase, the segregation of Cr and Ni is limited, and most of the preliminary δ-ferrite will transform into solid austenite finally. As a result, multi-branched shape crystals [51] generate without the formation of FQZ grains, as shown in Fig. 7(a) and (d).

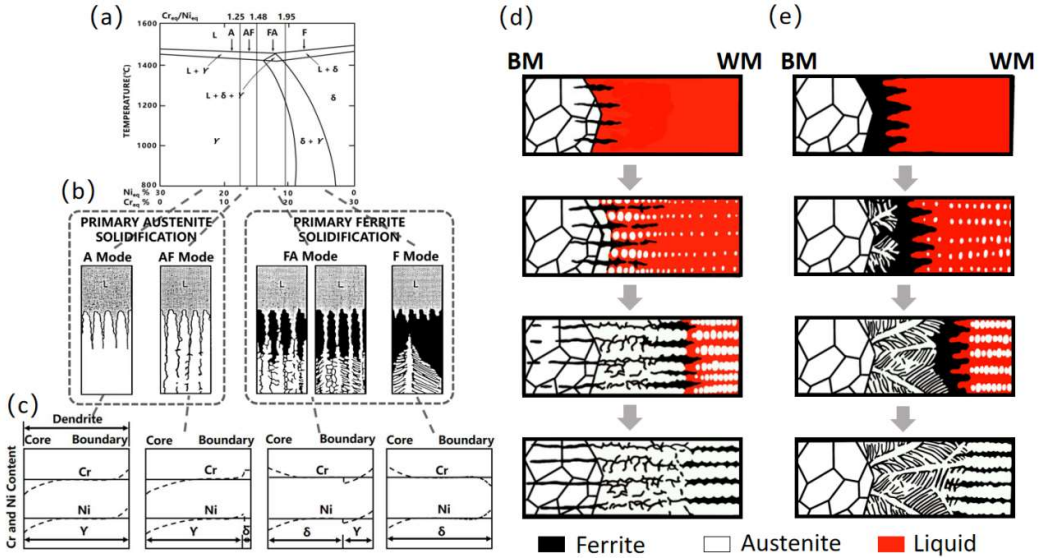

Fig. 15 (a) Pseudonymous section of the Fe-Cr-Ni ternary diagram at 70% Fe; (b) Corresponding solidification mode [24]; (c) Phase morphologies change with Ni_{eq}/Cr_{eq} content of in austenitic stainless steel welds showing [23][52]; (d) FA mode and (e) F mode crystal solidification microstructure of weld pool.

4.2 Effect of crystal orientation on mechanical properties

Slip and twinning are the two main plastic deformation mechanisms when metallic materials are under uniaxial tensile load. The crystals will deform in twinning when slip is obstructed. The orientation of the crystals does not alter when the crystals experience slip only. The critical resolved shear stress (CRSS) of twinning is much higher than that required for slip actuation, therefore, twinning is more likely to occurs at stress concentrations, while it is difficult for slip to happen. The formation

of the twin boundaries will prevent the dislocation movement and result in uniform stress distribution, therefore, twinning will take place and adjust crystal orientation [53].

As can be seen from Fig. 9(a), the crystal orientation of one side of the #1 weld deviates <001> and the other deviates <101>, as a result, a large angle grain boundary, formed in the <001> and <101> directions, appears in the middle of WM. Furthermore, large angle grain boundary parting lines tend to appear at FZs of the #2 and #3 welded joints, as shown in Fig. 8(b) and (c), and there is no large angle grain boundary displaying at the WMs, as shown in Fig. 9(b) and (c). Moreover, there is no obvious large angle grain boundary in WM and FZ regions of #4 welded joint, as shown in Fig. 8 (d) and Fig. 9 (d). Stress concentration always generates at the grain boundary as the dislocation movement is easily hindered by the large angle grain boundary under an external stress, then twins preferentially nucleate at the grain boundary and fracture takes place finally [54], thus resulting in the #1, #2, #3 and #4 welded joints failing under a uniaxial tensile stress fracture mechanism at WM, FZ, FZ and BM, respectively.

The dislocations in the welded joint under a uniaxial tensile stress easily move along the slip surface and will be pinned on encountering the obstacle of inconsistent deviation, thus resulting in stacking and entanglement. Afterwards it will be difficult for the dislocations to slip again and the crystal will undergo twinning deformation [55]. The orientation of crystals will be changed due to the formation of twins and further slipping will be stimulated, as a result, more energy will be consumed and the materials will show better plasticity [56] and dispersions on mechanical properties [57-60]. At the same time, the austenite grains are separated by deformation twins through acting in the role of subgrain boundaries, thus effectively preventing dislocation slip, leading to strain hardening effect and making the material present large tensile strength [61]. Despite the fact that there are large angle grain boundaries present at the FZs of the #2 and #3 welded joints (as shown in Fig. 8(b) and (c)), the grain size of the FZ is obviously smaller than that of the WM and the crystal anisotropy is obviously better than that at the WM of the #1 welded joint. Therefore,

it could be inferred that a small angle between the twin grain boundary stress direction of #2 and #3 welded joints and direction of uniaxial tension will be generated, which contributes to the slip of dislocation, but not for the generation of twins. Moreover, an internal shear stress in the welding joint results from the dislocation slip and will reduce the tensile strength of the material, thus explaining that the tensile strength of # 1 welded joint is much larger than that of #2, #3 and #4.

5 Conclusions

MAG welding was performed on four kinds of austenitic stainless steels and following conclusions can be drawn from the study of microstructure, mechanical properties and the material fracture mechanism:

(1) The welds of the four kinds of welded joints are composed of austenite and ferrite, and large angle grain boundaries are visible in the weld centre of 301L stainless steel. Large HAZ areas can be seen in the 304 and 316L welded joints, furthermore, large angle grain boundaries are present in the phase structure of the FZ area due to the generation of FQZ with high crack sensitivity. In addition, there is no obvious HAZ area appearing at the welded joints of 301L and 321.

(2) The results of uniaxial tension tests for the four kinds of austenitic stainless steels indicate that the tensile properties of 301L welded joints decrease significantly compared with that of the base metal, while the tensile properties of 304, 316L and 321 stainless steel welded joints are similar to that of the base metal. The 301L stainless steel welded joints fractures at the weld centre, and the fracture positions of the 304 and 316L welded joints are at the HAZ areas, while that for the 321 welded joint is in the base metal. Moreover, the hardness distribution curves of the four welded joints also indicate the same mechanical property law as that of uniaxial tension tests.

(3) The solidification modes in the welds of the four types of stainless steel are all AF mode, and the solidification modes in FZ areas are different. The solidification mode of 301L and 321 stainless steel is F mode, in which a large amount of ferrite precipitates. The energy can be effectively preserved by the precipitation ferrite, and a

FZ area with better anisotropy will be generated. Moreover, the solidification mode of 304 and 316L is FA mode. The heat conduction between the molten pool and the base metal cannot be inhibited, thus resulting in the formation of FQZ area and an obvious large angle crystal split line appears at FZ, which increases the critical shear stress during tension.

Future work

The solidification mode, microstructure and mechanical properties of the four welded joints under the same welding process had been studied in this manuscript, and their fracture mechanisms had been analyzed from the perspective of crystallography.Future work could be done as follows:

(1) The corrosion resistance of the four welded joints should be analyzed in detail, including the intergranular corrosion mechanism, electrochemical corrosion mechanism, etc. Then the service performance of the four stainless steel welded joints would be assessed in a field environment.

(2) In addition, the influence of different welding methods, welding process parameters and pre-welding heat treatment on the microstructure, mechanical properties and corrosion resistance of different stainless steel welded joints should be studied in detail.

Credit authorship contribution statement

Jihua Liu: Investigation, Data Curation, Methodology, Formal analysis, Writing-original draft.

Pijie Yu: Data Curation, Methodology, Formal analysis, Experimental samples preparation, Writing-original draft.

Peng Chen: Data Curation, Methodology, Formal analysis, Experimental samples preparation.

Shitao Chen: Methodology, Formal analysis, Experimental samples preparation.

Roger Lewis: Writing Review and Editing, Methodology, Formal analysis.

Zhibiao Xu: Methodology, Funding acquisition (partial).

Peng Li: Methodology, Formal analysis, Experimental samples preparation.

Chenggang He: Supervision, Methodology, Formal analysis, Writing Review and Editing, Funding acquisition.

Declaration of competing interest

The authors declare that they have no known competing financial interests or personal relationships that could have appeared to influence the work reported in this paper.

Acknowledgments

The work was supported by the Guangdong Basic and Applied Basic Research Foundation (No. 2019A1515110807), the Youth Innovation Talents Project of Guangdong Provincial Department of Education (No. 2018KQNCX271) and the General University Research Project of Recognized Category
(No. 2019GKQNCX104). Moreover, special thanks to the China Scholarship Council for providing financial support to visit the University of Sheffield, UK.

References

[1] H. Bhadeshia, R. Honeycombe. Steels: Microstructure and Properties. Butter worth-Heinemann Press. London, 2017: 343-376.
DOI:https://doi.org/10.1016/B978-0-08-100270-4.00012-3.

[2] K.H. Lo, C.H. Shek, J.K.L. Lai. Recent developments in stainless steels. Materials Science and Engineering: R, 2009,65: 39-104. DOI:https://doi.org/10.1016/j.mser.2009.03.001.

[3] L. Chen, G. Mi, X. Zhang, C. Wang. Numerical and experimental investigation on microstructure and residual stress of multi-pass hybrid laser-arc welded 316L steel. Materials & Design, 2019, 168: 107653. DOI: https://doi.org/10.1016/j.matdes.2019.107653.

[3] Z.W. Zhu, X.Q. Ma, C.M. Wang, G.Y, Mi. Grain refinement and orientation alternation of 10 mm 316L welds prepared by magnetic field assisted narrow gap laser-MIG hybrid welding. Materials Characterization, 2020, 164: 110311.
DOI: https://doi.org/10.1016/j.matchar.2020.110311.

[5] S. Liu, G. Mi, F. Yan, C. Wang, P. Jiang. Correlation of high power laser welding parameters with real weld geometry and microstructure. Optics & Laser Technology, 2017, 94: 59-67.
DOI: https://doi.org/10.1016/j.optlastec.2017.03.004.

[6] F. Wu, C. Chao, J. Fan. MAG welding process test of austenitic stainless steel, The 3rd Innovation Forum of Metal Processing Technology, 2021: 252-255. (in Chinese).
DOI: 10.26914/c.cnkihy.2021.047745.

[7] C.M. Zhang, W.W. Gao, W. Wei, Y.X. Chen. Plasma arc MAG composite welding process for butt welding of austenitic stainless steel sheet. Welding Technology, 2021, 35: 54-58. (in Chinese). DOI:10.13846/j.cnki.cn12-1070/tg.2022.03.019.
[8] Z.G. Liu, X.J. Zhou, T.T. Zhu, L. Chen, F. Chen, Q. Xu. Research status and prospect of A-TIG welding method. Materials Reports, 2021, 35: 353-357. (in Chinese).
[9] C. Meran, V. Kovan,A. Aiptekin. Friction stir welding of AISI 304 austenitic stainless steel. Materials Science& Engineering Technology. 2007, 38(10): 829-835. DOI:https://doi.org/10.1002/mawe.200700214.
[10] S. Celen, S. Karadeniz, H. Oezden. Effect of laser welding parameters on fusion zone morphological, mechanical and microstructural characteristics of AISI 304 stainless steel. Materials Science& Engineering Technology, 2008, 39(11): 845-850. DOI:https://doi.org/10.1002/mawe.200800384.
[11] J. Xu, Y.O. Xiang, H.Y. Pei, W., Song. High-cycle and very-high-cycle fatigue behavior of a stainless steel for air-conditioning compressor valve plates. International Journal of Structural Integrity, 2022, 13(2): 185-195. DOI: https://doi.org/10.1108/IJSI-10-2021-0108
[12] X. Liu, Y. Zhang, S. Xie, Q.Zhang, H. Guo. Fatigue failure analysis of express freight sliding side covered wagon based on the rigid-flexibility model. International Journal of Structural Integrity, 2021, 12(1): 98-108. DOI: https://doi.org/10.1108/IJSI-11-2019-0122
[13] M.P. Singh,D.K. Shukla, R. Kumar, K.S. Arora. The structural integrity of high-strength welded pipeline steels: a review. International Journal of Structural Integrity, 2021, 12(3): 470-496. DOI: https://doi.org/10.1108/IJSI-05-2020-0051
[14] H.X. Zong. Effect of different protective atmosphere on microstructure and properties of 06Cr19Ni10 stainless steel MAG welding joints. Master's thesis, Dalian Jiaotong University, Dalian, 2018. (in Chinese)
[15] C.C. Guo. Study on butt welding process of S355J2W+N weather-resistant steel plate by high frequency pulse MAG welding. Master's thesis, Dalian Jiaotong University, Dalian, 2020. (in Chinese)
[16] A. Scotti, V. Ponomarev, W. Lucas. A scientific application oriented classification for metal transfer modes in GMA welding. Journal of Materials Processing Technology, 2012, 212(6), 1406-1413. DOI:https://doi.org/10.1016/j.jmatprotec.2012.01.021.
[17] D. Iordachescu, L.Quintino. Steps toward a new classification of metal transfer in gas metal arc welding. Journal of Materials Processing Technology, 2008, 202(1-3): 391-397. DOI:https://doi.org/10.1016/j.jmatprotec.2007.08.081.
[18] R.S. Huang, L. Kang, X. Ma. Microstructure and phase composition of a low-power YAG laser-MAG welded stainless steel joint. Journal of Materials Engineering and Performance, 2008, 17: 928-935. DOI:https://doi.org/10.1007/s11665-008-9241-5.
[19] R. Unnikrishnan, K.S.N. Satish Idury, T.P. Ismail, A. Bhadauria, S.K. Shekhawat, R.K. Khatirkar, S.G. Sapate. Effect of heat input on the microstructure, residual stresses and corrosion resistance of 304L austenitic stainless steel weldments. Materials Characterization, 2014, 93: 10-23. DOI:https://doi.org/10.1016/j.matchar.2014.03.013.
[20] P. Luchtenberg, P.T. Campos, P. Soares, C.A.H Laurindo, O. Maranho, R.D. Torres. Effect of welding energy on the corrosion and tribological properties of duplex stainless steel weld overlay deposited by GMAW/CMT process. Surface and Coatings Technology, 2019, 375: 688-693. DOI:https://doi.org/10.1016/j.surfcoat.2019.07.072.

[21] W.K. Xiao, L. Zhu, F.j. Zhang, K.S. Dai, X. Zai, X. Yang, B.J. Chen. Effect of heat input on cryogenic toughness of 316LN austenitic stainless steel NG-MAG welding joints with large thickness. Materials & Design, 2015, 86: 160-167.
DOI:https://doi.org/10.1016/j.matdes.2015.07.115.
[22] M.J. Cieslak, A.M. Ritter, W.F. Savage. Solidification cracking and analytical electron microscopy of austenitic stainless steel weld metals. The Welding Journal, Jan, 1982, 1-8.
[23] V. Shankar, T.P.S. Gill, S.L. Mannan, S. Sundaresan. Solidification cracking in austenitic stainless steel welds. Sadhana, 2003, 28: 3-4. DOI:https://doi.org/10.1007/BF02706438.
[24] J.C. Simmons, X.B. Chen, A. Azizi, M.A. Daeumer, P.Y. Zavalij, G.W. Zhou, S.N. Schiffres. Influence of processing and microstructure on the local and bulk thermal conductivity of selective laser melted 316L stainless steel. Additive Manufacturing, 2020, 32: 100996.
DOI:https://doi.org/10.1016/j.addma.2019.100996.
[25] GB/T 985.1-2008. Recommended joint preparation for gas welding, manual metal arc welding, gas-shield arc welding and beam welding. 2008. (in Chinese).
[26] L. Chen, C.M. Wang, X. Zhang, G.Y. Mi. Effect of parameters on microstructure and mechanical property of dissimilar joints between 316L stainless steel and GH909 alloy by laser welding. Journal of Manufacturing Processes, 2021, 65:60-69.
DOI: https://doi.org/10.1016/j.jmapro.2021.03.015.
[27] P.Y. Dai, S. Li, L. Wu, Y.F Wang, G.J. Feng, D.A. Deng. A new numerical model to predict welding-induced sensitization in SUS304 austenitic stainless steel joint. Journal of Materials Research and Technology, 2022, 17:234-243. DOI: https://doi.org/10.1016/j.jmrt.2022.01.015.
[28] P. Jiang, S. Gao, S.N. Geng, C. Han, G.Y. M. Multi-physics multi-scale simulation of the solidification process in the molten pool during laser welding of aluminum alloys. International Journal of Heat and Mass Transfer, 2020, 161:120316.
DOI: https://doi.org/10.1016/j.ijheatmasstransfer.2020.120316.
[29] A.Sriba, J.B.Vogt. Galvanic coupling effect on pitting corrosion of 316L austenitic stainless steel welded joints. Metals and Materials International, 2021, 27: 5258-5267.
DOI:https://doi.org/10.1007/s12540-020-00789-4.
[30] R. Kumar, J.S. Chohan, R. Goyal, P. Chauhan. Impact of process parameters of resistance spot welding on mechanical properties and micro hardness of stainless steel 304 weldments. International Journal of Structural Integrity, 2021, 12(3): 366-377.
DOI: https://doi.org/10.1108/IJSI-03-2020-0031.
[31] Y.H. Guo, D. Deng, Z.Z. Sun, B.C. Huang. Microstructure and mechanical properties of heat-affected zone of repeated welding on 304 stainless steel. Nuclear Power Engineering, 2021, 42: 1-6. (in Chinese) DOI: 10.13832/j.jnpe.2021.04.0198
[32] G.Green, R. Higginson, S. Hogg, S. Spindler, C. Hamm, J.Najorka. Analysis of ferrite formed in 321 grade austenitic stainless steel. Materials Science and Technology, 2015, 31(4): 418-425.
DOI:https://doi.org/10.1179/1743284714Y.0000000564.
[33] Y.N. Hu, S.C. Wu, Y. Guo, S. Zhao, A.M. Korsunsky, Y.K. Yu, X. Zhang, Y.N. Fu, Z.G. Che, T.Q. Xiao, S. Lozano-Perez, Q.X. Yuan, X.L. Zhong, X.Q. Zeng, G.Z. Kang, P.J. Withers. Inhibiting weld cracking in high-strength aluminium alloys. Nature Communications, 2022, 13, 5816. DOI:https://doi.org/10.1038/s41467-022-33188-x.

[34] J.H. Liu, X.H. Li, Y.J. Zhou, P.J. Yu, C.G. He, Z.B. Xu. Microstructure and mechanical properties of active gas arc welding between 304 austenitic stainless steel and Q235B low carbon steel. Journal of Materials Engineering and Performance, 2022, 1-8.
DOI:https://doi.org/10.1007/s11665-022-06808-2.
[35] S.Q. Chen, X. Wei, J.K. Zhao, H. Wang. Study on microstructure and mechanical properties of laser welded joint of 6mm thick 304 austenitic stainless steel. Mchinery Design & Manufacture, 2021, 6(5): 139-142. (in Chinese), DOI: 10.19356/j.cnki.1001-3997.2021.06.032.

[36] V. García-García, F. Reyes-Calderón, O.D. Frasco-García, N. Alcantar-Modragón. Mechanical behavior of austenitic stainless-steel welds with variable content of δ-ferrite in the heat-affected zone. Engineering Failure Analysis, 2022, 140: 106618.
DOI:https://doi.org/10.1016/j.engfailanal.2022.106618.
[37] H.X. Wang, Y.X. Wang, X. Li, W.Q. Wang, X.W. Yang. Influence of assembly gap size on the structure and properties of SUS301L stainless steel laser welded lap joint. Materials, 2021, 14: 996. (in Chinese) DOI: https://doi.org/10.3390/ma14040996.
[38] Y.S. Hao, J. Li, X. Li, W.C. Liu, G.M. Cao, C.G. Li, Z.Y. Liu. Influences of cooling rates on solidification and segregation characteristics of Fe-Cr-Ni-Mo-N super austenitic stainless steel. Journal of Materials Processing Technology, 2020, 275: 116326.
DOI: https://doi.org/10.1016/j.jmatprotec.2019.116326.
[39] C.L. Zhou, P.Z. Dai, H. Wu, M.H. He, X.H. Liu, P.K. Chu. Effect of the ferrite morphology on hydrogen embrittlement of MAG welded 304 austenitic stainless steel. Applied Surface Science, 2022, 606: 154866.DOI: https://doi.org/10.1016/j.apsusc.2022.154866.
[40] L. Zhang, J.Z. Lu, K.Y. Luo, A.X. Feng, F.Z. Dai, J.S. Zhong, M. Luo, Y.K. Zhang. Residual stress, micro-hardness and tensile properties of ANSI 304 stainless steel thick sheet by fiber laser welding. Materials Science and Engineering A, 2013, 561: 136-144.
DOI:https://doi.org/10.1016/j.msea.2012.11.001.
[41] M. Yan, M.Y. Wang, Z.F. Xu, Y. Liu, L. Chen, H.G. Huang. Analysis on the bending deformation characteristic and crack failure mechanism of thin-walled stainless-steel bellows. Engineering Failure Analysis, 2023, 143: 106900.
DOI:https://doi.org/10.1016/j.engfailanal.2022.106900.
[42] C. Qian, J. Liang, Y.F. Huang, J.D. Kang, J. Gianetto. A comparative study on constraint parameters for characterizing fracture toughness of X60 and X100 pipe steels. Engineering Failure Analysis, 2022, 141: 1350-6307. DOI: https://doi.org/10.1016/j.engfailanal.2022.106617.
[43] D.D. Gu, H.Y. Chen. Selective laser melting of high strength and toughness stainless steel parts: The roles of laser hatch style and part placement strategy. Materials Science and Engineering A, 2018, 725: 419-427.
DOI: https://doi.org/10.1016/j.msea.2018.04.046.
[44] L.Q. Tang, C.F. Qian, A. Ince, J. Zheng, H.F. Li, Z.C. Han. Fatigue crack growth behavior of the MIG welded joint of 06Cr19Ni10 stainless steel. Materials, 2018, 11(8): 1336.
DOI: https://doi.org/10.3390/ma11081336.
[45] S. Roychowdhury, V. Kain, A. Matcheswala, A. Bhandakkar. σ-Phase induced embrittlement in titanium containing austenitic stainless steel tie-bars in a condenser. Engineering Failure Analysis, 2012, 25: 123-132.DOI: https://doi.org/10.1016/j.engfailanal.2012.05.002.

[46] R. Rajasekaran, A.K. Lakshminarayanan, R. Damodaram, V. Balasubramanian. Stress corrosion cracking failure of friction stir welded nuclear grade austenitic stainless steel. Engineering Failure Analysis, 2021, 120: 105012.
DOI: https://doi.org/10.1016/j.engfailanal.2020.105012.
[47] Y.N. Li, D.N. Zou, W.W. Chen, Y.B, Zhang, W. Zhang, F.H. Xu. Effect of Cooling Rate on Solidification and Segregation Characteristics of 904L Super Austenitic Stainless Steel. Metals and Materials International, 2022, 28(): 1970-1918.
DOI: https://doi.org/10.1007/s12540-021-01091-7.
[48] F.X. Huang, X.H. Wang, J.M. Zhang, C.X. Ji, Y. Fang, Y. Yu. In Situ Observation of Solidification Process of AISI 304 Austenitic Stainless Steel. Journal of Iron and Steel Research International, 2008, 15(6): 78-82.DOI: https://doi.org/10.1016/S1006-706X(08)60271-X.
[49] W. Martienssen,H. Warlimont. Springer handbook of condensed matter and materials data, Springer Berlin Heidelberg Press. Berlin, 2006: 221-268.
[50] N. Mao. Microstructure and mechanical properties of welded joint of 316L stainless steel, Master's thesis, Harbin Institute of Technology. Harbin, 2012. (in Chinese)
[51] N.Suutala. Effect of solidification conditions on the solidification mode in austenitic stainless steels. Metallurgical Transactions A, 1983, 14: 191-197.
DOI: https://doi.org/10.1007/BF02651615.
[52] L.J. Shen. Microstructure transformation of 0Cr18Ni9 austenite stainless steel under solidification, Master's thesis, Inner Mongolia University of Science & Technology. Baotou, 2012. (in Chinese)
[53] C.F. Yu, C.C. Zhao, Z.F. Zhang, W. Liu. Tensile properties of selective laser melted316L stainless steel. Acta Metallurgica Sinica, 2020, 56(5): 683-692.
DOI: 10.11900/0412.1961.2019.00278.
[54] C.U. Jeong, W. Woo, J.Y. Choi, S.-H. Choi. Effect of kinematic stability of initial orientation on deformation heterogeneity and ductile failure in duplex stainless steel during uniaxial tension. Acta Materialia, 2014, 67: 21-31.
DOI: https://doi.org/10.1016/j.actamat.2013.12.020.
[55] L. Xiong, Z.S. You, S.D. Qu, L. Lu. Fracture behavior of heterogeneous nanostructured 316L austenitic stainless steel with nanotwin bundles. Acta Materialia, 2018, 150: 130-138.
DOI: https://doi.org/10.1016/j.actamat.2018.02.06.
[56] R.D.K. Misra, S. Nayak, S.A. Mali, J.S. Shah, M.C. Somani, L.P. Karjalainen. On the significance of nature of strain-induced martensite on phase-reversion-induced nanograined/ultrafine-grained austenitic stainless steel. Metallurgical and Materials Transactions A, 2010, 41(3): 3-12.DOI: https://doi.org/10.1007/s11661-009-0072-2.
[57] D. Liao, S.P. Zhu, B. Keshtegar, G. Qian, Q.Y. Wang. Probabilistic framework for fatigue life assessment of notched components under size effects. International Journal of Mechanical Sciences, 2020, 181: 105685. DOI: https://doi.org/10.1016/j.ijmecsci.2020.105685
[58] S.P. Zhu, Q. Liu, W. Peng, X.C. Zhang. Computational-experimental approaches for fatigue reliability assessment of turbine bladed disks. International Journal of Mechanical Sciences, 2018, 142-143: 502-517. DOI: https://doi.org/10.1016/j.ijmecsci.2018.04.050.
[59] S.P. Zhu, S. Foletti, S. Beretta. Probabilistic framework for multiaxial LCF assessment under material variability. International Journal of Fatigue, 2017, 103: 371-385.
DOI: https://doi.org/10.1016/j.ijfatigue.2017.06.019.

[60] X.P. Niu, R.Z. Wang, D. Liao, S.P. Zhu, X.C. Zhang, B. Keshtegar. Probabilistic modeling of uncertainties in fatigue reliability analysis of turbine bladed disks. International Journal of Fatigue, 2021, 142: 105912. DOI: https://doi.org/10.1016/j.ijfatigue.2020.105912.
[61] F.K. Yan, G.Z. Liu, N.R. Tao, K. Lu. Strength and ductility of 316L austenitic stainless steel strengthened by nano-scale twin bundles. Acta Materialia, 2012, 60(3): 1059-1071.
DOI: https://doi.org/10.1016/j.actamat.2011.11.009.